Influence of Anthropogenic Warming on the Atlantic Multidecadal Variability and Its Impact on Global Climate in the Twenty-First Century in the MPI-GE Simulations

Minhua Qin,[a,b] Aiguo Dai,[c] and Wenjian Hua[b]

[a] Department of Atmospheric and Oceanic Sciences and Institute of Atmospheric Sciences, Fudan University, Shanghai, China
[b] Key Laboratory of Meteorological Disaster, Ministry of Education (KLME)/Joint International Research Laboratory of Climate and Environment Change (ILCEC)/Collaborative Innovation Center on Forecast and Evaluation of Meteorological Disasters (CIC-FEMD), Nanjing University of Information Science and Technology, Nanjing, China
[c] Department of Atmospheric and Environmental Sciences, University at Albany, State University of New York, Albany, New York

ABSTRACT: The Atlantic multidecadal variability (AMV), a dominant mode of multidecadal variations in North Atlantic sea surface temperatures (NASST), has major impacts on global climate. Given that both internal variability and external forcing have contributed to the historical AMV, how future anthropogenic forcing may regulate the AMV is of concern but remains unclear. By analyzing observations and a large ensemble of model simulations [i.e., the Max Planck Institute Grand Ensemble (MPI-GE)], the internally generated (AMV_{IV}) and externally forced (AMV_{EX}) components of the AMV and their climatic impacts during the twenty-first century are examined. Consistent with previous findings, the AMV_{IV} would weaken with future warming by 11%–17% in its amplitude by the end of the twenty-first century, along with reduced warming anomaly over the midlatitude North Atlantic under future warming during the positive AMV_{IV} phases. In contrast, the AMV_{EX} is projected to strengthen with reduced frequency under future warming. Furthermore, future AMV_{IV}-related temperature variations would weaken over Eurasia and North Africa but strengthen over the United States, whereas AMV_{IV}-related precipitation over parts of North America and Eurasia would weaken in a warmer climate. The AMV_{EX}'s impact on global precipitation would also weaken. The results provide new evidence that future anthropogenic forcing (i.e., nonlinear changes in GHGs and aerosols) under different scenarios can generate distinct multi-decadal variations and influence the internally generated AMV, and that multidecadal changes in anthropogenic forcing are important for future AMV.

KEYWORDS: Atlantic Ocean; Anthropogenic effects/forcing; Climate models; Multidecadal variability

1. Introduction

The Atlantic multidecadal variability (AMV) refers to the multidecadal (60–80 yr) sea surface temperature (SST) variations across the North Atlantic Ocean (Schlesinger and Ramankutty 1994; Kushnir 1994; Kerr 2000). The AMV can cause significant multidecadal climate fluctuations in many regions across the globe (O'Reilly et al. 2017; Ruprich-Robert et al. 2017; Hua et al. 2021). The positive phase of the AMV is usually associated with warm, dry summers over North America (Enfield et al. 2001; Sutton and Hodson 2005; Ruprich-Robert et al. 2018), wet summers over northern Europe (Sutton and Dong 2012; Qasmi et al. 2017; Ghosh et al. 2017), strong Asian summer monsoons (Lu et al. 2006) and warming over Northeast Asia (Hua et al. 2021; Monerie et al. 2021), a wet Sahel region and dry South America (Folland et al. 1986; Knight et al. 2006; Martin et al. 2014; Hua et al. 2019), and an increase of intense Atlantic hurricane activity (Zhang and Delworth 2006; Wang et al. 2012). In some cases, the AMV's influence may have dominated over the anthropogenic signal so far (Chylek et al. 2014). Given the AMV's major climatic impacts around the world, understanding the physical processes that drive the

AMV and its future response to global warming is a key challenge in climate research.

The AMV is generally thought to naturally arise from air–sea interactions and ocean circulation, namely the Atlantic meridional overturning circulation (AMOC) (Delworth and Mann 2000; Knight et al. 2005; Zhang et al. 2019). Atmospheric forcing is also considered as an important contributor to the North Atlantic SST (NASST) variability (Clement et al. 2015; Sun et al. 2015; Delworth and Zeng 2016; Delworth et al. 2017). Besides the internal variations in the climate system, external forcing, such as decadal variations in natural and anthropogenic aerosols, may also contribute to the observed AMV since the late nineteenth century (Mann and Emanuel 2006; Booth et al. 2012; Murphy et al. 2017; Bellucci et al. 2017; Bellomo et al. 2018; Hua et al. 2019; Watanabe and Tatebe 2019; Haustein et al. 2019; Qin et al. 2020a). Thus, the observed AMV should be viewed as a combination of both internal variability and response to external forcing (Ting et al. 2009; Otterå et al. 2010; Terray 2012; Tandon and Kushner 2015; Si and Hu 2017; Qin et al. 2020b). Booth (2015) and Steinman et al. (2015) suggested using the term Atlantic multidecadal oscillation (AMO) to refer to the internal component of the NASST multidecadal variations only and the term AMV to depict the total multidecadal variations in NASSTs from both internal variability and external forcing to avoid confusion. Here, we use AMV_{IV} and AMV_{EX} to

Corresponding authors: Wenjian Hua, wenjian@nuist.edu.cn; Aiguo Dai, adai@albany.edu

explicitly represent, respectively, the internally generated and externally forced components of the AMV.

Much attention has been given to the climatic impacts and the underlying mechanisms of the historical AMV. Given the significant contributions by historical external forcing to the AMV and the possibility that future warming may alter AMV_{IV} and generate new AMV_{EX}, we wonder what future AMV may look like and how it may affect regional climates over the globe by the end of the twenty-first century. Future anthropogenic climate change may affect internal climate modes, such as the interdecadal Pacific oscillation (IPO) (Xu and Hu 2018; Wu et al. 2018; Wu and Liu 2020), El Niño–Southern Oscillation (ENSO) (Collins et al. 2010; Cai et al. 2015), and AMO (Wu et al. 2018; Wu and Liu 2020). For example, the IPO is projected to have a weaker amplitude, higher frequency, and a muted impact on North American temperature and precipitation in a warmer climate (Xu and Hu 2018; Wu et al. 2018; Wu and Liu 2020), and the AMV's amplitude is also projected to decrease in future warmer climates (Wu et al. 2018; Wu and Liu 2020). Models also project a weakened AMOC and weak warming or slight cooling in the subpolar North Atlantic Ocean in the twenty-first century (Collins et al. 2013), and the AMOC's multidecadal amplitude and period are also projected to decrease (Drijfhout et al. 2008; Cheng et al. 2016). The weakened AMOC contributes to the surface ocean cooling south of Greenland [i.e., the North Atlantic warming hole (NAWH)] and a reduced Arctic sea ice loss (Dai et al. 2005; Liu et al. 2020). Given that the AMOC affects NASST and is likely a key driver of the AMV (Zhang et al. 2019), one might expect future AMV to change due to the weakened AMOC. Recently, Wu and Liu (2020) suggested that the intensified warming by the twenty-third century leads to a decrease in the AMV's amplitude, resulting in reduced multidecadal variability in NASST, which is consistent with the reduced amplitude in the AMOC's multidecadal variability (Drijfhout et al. 2008; Cheng et al. 2016). However, the quantification of the AMV depends on its index, which is sensitive to the detrending method used to remove the long-term nonlinear trend (Qin et al. 2020b). This is particular true under future scenarios where the internal variability and changes caused by nonlinear external forcing mix with each other. Previous studies (Wu et al. 2018; Wu and Liu 2020) derived the future AMV index simply by using area-weighted averaging of smoothed NASST anomalies relative to its long-term linear trend (Enfield et al. 2001). Clearly, this does not cleanly remove externally forced decadal–multidecadal changes from the internally generated variations, as the externally forced changes are nonlinear (Qin et al. 2020b). As a result, previous reported future AMV changes may result from both internal variability change and externally forced signal. Thus, it is still unclear how much of the reported future AMV change is due to changes in internal variability or externally forced response. Furthermore, it is unknown how the future AMV_{IV} and AMV_{EX} components of the AMV may affect regional climates over the globe in the twenty-first century under global warming.

Given the AMV's long time scales, separating the forced response from internal variability in NASST is challenging

(Vecchi et al. 2017; Qin et al. 2020a,b). To reduce the chance of aliasing between AMV_{IV} and AMV_{EX}, an effective way is to use the multimodel ensemble mean (MMM) as the estimate of the forced signal and remove it from the observations or individual model simulations (Dai et al. 2015; Steinman et al. 2015; Frankcombe et al. 2015; Hua et al. 2018; Qin et al. 2020b). As the different rates of anthropogenic warming among the models can cause their trajectories of the forced response to diverge and differ from MMM (Frankcombe et al. 2018), the MMM may not be the true forced signal in individual model runs. Another way is to create a large ensemble of simulations with a single climate model (Kay et al. 2015; Dai and Bloecker 2019) and use the single-model ensemble mean as the forced signal. Using large ensembles from multiple models (Deser et al. 2020) can allow us to effectively separate the forced response from internal variability and provide a range of the forced response at the same time.

This study aims to quantify the influence of anthropogenic warming in the twenty-first century on the internally generated and externally forced components of the AMV and their impacts on global climate through analyses of a single-model large ensemble simulations from the Max Planck Institute Grand Ensemble (MPI-GE). MPI-GE is the largest ensemble (with 100 members) from a single climate model currently available. We apply an improved procedure to separate the AMV_{IV} and AMV_{EX} components in observations and model simulations and examine their future changes. Moreover, we investigate how the AMV and its influence on global climate would evolve in a future warmer climate using revised AMV indices that represent the internally generated multidecadal variability and externally forced changes in NASST. Our results should improve current understanding of the future AMV and its impacts on global climate.

2. Data, model simulations, and methods

a. Data and model simulations

We used the observational monthly SST data from 1870 to 2018 from the Hadley Centre Sea Ice and Sea Surface Temperature (HadISST) dataset on a 1° grid (Rayner et al. 2003). We also used the monthly surface temperature data from 1870 to 2018 on a 5° grid from HadCRUT4, which combined the observed surface air temperature over land and the SST over oceans (Morice et al. 2012). Small data gaps in HadCRUT4 were filled using spatial bilinear interpolation following Dai et al. (2015). We also used monthly precipitation data over land on a 1° grid derived from rain gauge observations from 1901 to 2018 from the Global Precipitation Climatology Centre (GPCC) Full Data Product V2018 (Schneider et al. 2014). To represent the future evolution of external forcing, we used the atmospheric CO_2 and sulfate aerosol concentrations under future representative concentration pathway (RCP) scenarios (https://tntcat.iiasa.ac.at/RcpDb/).

We analyzed the model simulations from the MPI-GE (Maher et al. 2019). MPI-GE is the largest ensemble of a single climate model (i.e., MPI-ESM1.1; Giorgetta et al. 2013) currently available, which includes a 2000-yr preindustrial

(PI) control run (with all forcing kept at the 1850 level), and a 100-member ensemble of simulations under the historical all-forcing (1850–2005) and under each of the future RCP scenarios (i.e., RCP2.6, RCP4.5, and RCP8.5) from 2006 to 2099, and a 100-member ensemble of 150-yr simulations with 1% CO_2 increase per year (1pctCO2) from the preindustrial level to an approximate quadrupling. The MPI-ESM1.1 model has an equilibrium climate sensitivity of 2.8°C and the global mean surface temperature increases by ~4.0°C at the end of the twenty-first century under RCP8.5 (Maher et al. 2019). Each of the 100 ensemble simulations has the same external forcing but starts from slightly perturbed initial conditions that often lead to different and thus uncorrelated realizations of the internal variability among the ensemble members. More information on these model simulations and their evaluation can be found in Maher et al. (2019). The model's ability to simulate the AMV is examined below.

b. Analysis methods

For our analysis, we need to first define the total nonlinear variations in NASST and then its externally forced and internally generated components. Some previous studies (e.g., Trenberth and Shea 2006) combined these two steps into one by removing the global-mean SST from NASST, with the resultant AMV index containing both forced and unforced components. Other studies (e.g., Deser and Phillips 2021) focused on the spatial patterns of the AMV, rather than the temporal variations of the AMV examined here. Because statistical methods alone cannot distinguish the physical origin of a signal, we will have to rely on the model ensemble mean to separate the forced and unforced components.

By definition, an oscillation is the deviation from the long-term mean (for a stationary series) or the long-term trend (for nonstationary series). Thus, the simplest method to derive an AMV index is to remove the long-term linear trend from annual NASST and temporally smooth it to remove variations on shorter time scales (Enfield et al. 2001). Such an AMV index includes both internally generated variations and externally forced changes. For example, nonlinear changes in historical and future greenhouse gases and aerosols can produce nonlinear multidecadal variations in NASST, and such forced variations can be mixed up with internally generated oscillations (Qin et al. 2020b). Because of their different nature of origin, it is important to quantify these two different components in the AMV for both the historical (Qin et al. 2020b) and future periods. Please note that we linearly detrended the forced time series in order to focus on the forced nonlinear component that can contribute to the AMV seen in individual model runs. Tests with other detrending methods, such as the ensemble empirical mode decomposition (EEMD; Wu and Huang 2009), to remove the effect of the long-term trend yield similar results. The forced multidecadal variations do not include the changes associated with the long-term trend and thus they should not be compared with model-projected total SST and other changes reported elsewhere.

We use the MPI-GE ensemble mean of all-forcing simulations to estimate and define the forced component in NASST, and then remove this forced component to define the internal variability in each ensemble simulation. The ensemble mean of a large ensemble from a single model [i.e., a single model ensemble mean (SMM)] can effectively remove the internal variations and provide an estimate of the forced component in NASST (Frankcombe et al. 2018), albeit it is based on one single model and thus may not be representative of the response in other models under the same forcing. On the other hand, the SMM can help us better quantify the internal variability than the multimodel ensemble, as the latter also contains intermodel spreads (Kay et al. 2015; Dai and Bloecker 2019; Deser et al. 2020).

To separate the internally generated and externally forced variations in observed NASST from 1870 to 2018, we used the MPI-GE ensemble mean at each grid point as the first-order estimate of the local forced signal (which may be nonlinear) and removed it through regression from the observed SST time series to produce the residual SST fields that contain primarily internal climate variations. We also used the global-mean SST (GMSST) from the ensemble mean of all-forcing historical simulations by MPI-GE as the estimate of the externally forced signal following Dai et al. (2015). The two methods produced similar results (not shown). An AMV index of the internally generated AMV (i.e., AMV_{IV}) is then obtained as the low-pass filtered area-weighted average of the residual SSTs over the North Atlantic (80°–0°W, 0°–60°N) from 1870 to 2018. For observations, we linearly detrended NASST locally over 1870–2018 and averaged it over the North Atlantic to derive the total AMV index (i.e., $AMV_{detrend}$), which contains both the forced and unforced components. A Lanczos low-pass filter with 19 annual data points and a 13-yr half-response period (Hua et al. 2018) is used in the low-pass filtering for both $AMV_{detrend}$ and AMV_{IV}, and the $AMV_{detrend}$ minus AMV_{IV} difference is used as the AMV_{EX} index, which represents the externally forced component in the $AMV_{detrend}$ from observations. The result is similar when using the linearly detrended, low-pass filtered NASST derived from the SMM to define the AMV_{EX}. For the model-simulated AMV indices (i.e., AMV_{IV}, AMV_{EX}) from 1870 to 2018, we used the arithmetic mean of the 100 members from the MPI-GE at each grid point as the estimate of the forced signal (used to create AMV_{EX}) and removed it directly (i.e., without regression) from individual members to produce the residual fields that contain primarily internal variations and used to create the AMV_{IV}. Since no external forcing is included in the PI control run, its AMV index purely represents the internal multidecadal variations in NASST (i.e., AMV_{IV}). Please note that we used linear detrending only to define the total nonlinear variations in NASST (i.e., $AMV_{detrend}$), and its forced component AMV_{EX} was derived using the MPI-GE ensemble mean time series. As a test, we also used the EEMD method to derive the long-term trend for defining the total AMV (i.e., $AMV_{detrend}$) instead of the linear detrending. The results are similar (not shown).

To further examine whether the AMV indices (including the AMV_{IV} and AMV_{EX}) change over time under global warming in the MPI-GE, we calculate the annual AMV_{EX} (same for all runs) and AMV_{IV} (different among ensemble members) indices for 1906–99 and 2006–99, respectively.
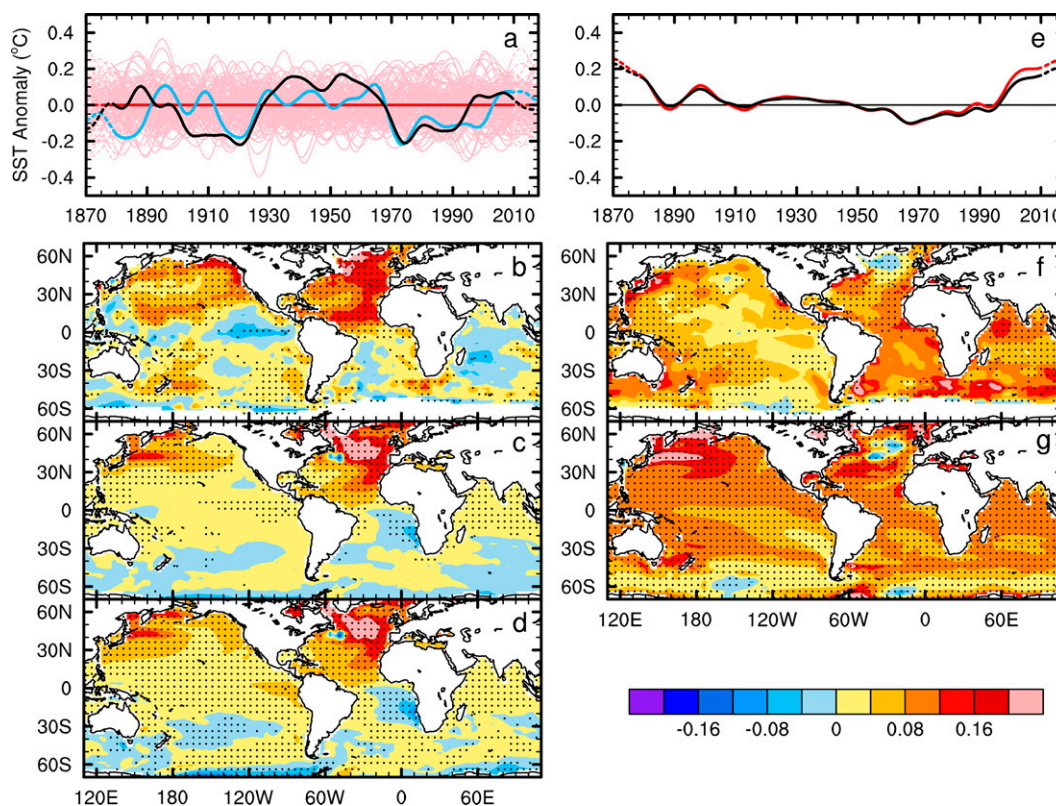
FIG. 1. Temporal and spatial patterns of the AMV_{IV} and AMV_{EX} from 1870 to 2018 in observations and models. (a) Time series of the AMV_{IV} indices for 1870–2018 from individual model runs (pink) from MPI-GE and their ensemble mean (red), compared with that from observations (black) (the zero line is for the 1901–70 mean, and likewise for other panels in this figure). The blue line is the AMV_{IV} index from one model run (#55, which is similar to the observations). The data near the two ends are derived with mirrored data in the filtering and thus are less reliable; they are represented by dashed lines. (b) Spatial regression pattern (°C per one standard deviation of the AMV_{IV} index) obtained by regressing the low-pass filtered local SST anomalies onto the standardized AMV_{IV} index from observations during 1870–2018. (c) As in (b), but for ensemble-averaged SST regression patterns from the individual historical simulations from MPI-GE. (d) As in (c), but derived from the MPI-GE preindustrial control simulation. (e)–(g) As in (a)–(c), but for the AMV_{EX} index [black for observations and red for model simulations in (e)] and its associated SST regression pattern from observations and historical simulations. The stippling in (b), (d), (f), and (g) indicates that the anomalies are statistically significant at the 0.05 level based on a Student's *t* test considering autocorrelation, while the stippling in (c) represents 67 out of the 100 runs showing the same sign.

Here we detrended NASST locally and separately over 1906–99 and 2006–99, as the historical and future trends differ substantially, and averaged the detrended SST fields for the forced signal and the residual to derive the model AMV_{IV}. For the historical period from 1870 to 2018, the AMV_{EX} is similar when detrending the principal component of the leading EOF of the forced SST fields over the North Atlantic, which accounts for 95% of the variance and shows a spatial pattern similar to historical AMV (figure not shown).

For the model simulations, we defined an AMOC index as an average of the meridional overturning streamfunction over a fixed region (20°–50°N and 500–2000-m depth) that contains the maximum streamfunction. The results are similar when using the maximum of the meridional overturning streamfunction in the Atlantic basin between 20° and 80°N around 500–6000-m depth as done in Delworth and Dixon (2006) and Cheng et al. (2016); however, the location of the maximum

may change over time so that the temporal variations of the maximum include contributions from spatial changes. To derive the common external component ($AMOC_{EX}$, with its linear trend removed) and the individual internal variations ($AMOC_{IV}$) of the AMOC in the historical and future RCP8.5 simulations (MPI-GE does not provide the meridional overturning circulation data under the RCP2.6 and RCP4.5 scenarios), we used the MPI-GE ensemble mean of the streamfunction as the estimate of the forced signal and removed it from individual model runs to produce the residual fields that represent the $AMOC_{IV}$. Thus, the $AMOC_{EX}$ and $AMOC_{IV}$ indices represent, respectively, the externally forced and internally generated multidecadal variations of the AMOC.

Each of the 100 members from MPI-GE randomly samples the internal AMO cycles (i.e., AMV_{IV}) over a 250-yr period (from 1850 to 2099) under one of the future RCP scenarios from 2006 to 2099 (but with the same historical all-forcing
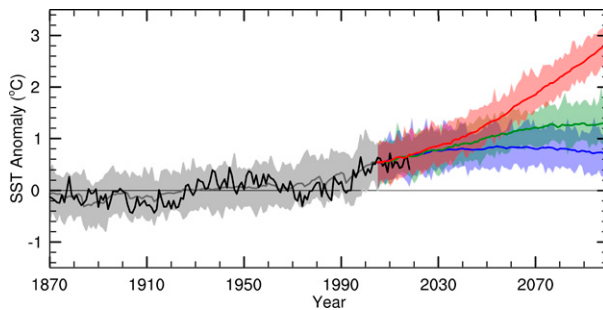
FIG. 2. Historical and future changes in NASST from observations and models. Time series of annual SST anomalies (°C; relative to the mean of 1901–70) averaged over the North Atlantic (80°W–0°, 0°–60°N) from observations (from HadISST1; black line) for 1870–2018, and model simulations from MPI-GE. The ensemble spread (shading) and ensemble mean (thick lines) are shown for the historical (1870–2005; gray) and future (2006–99) simulations under the low RCP2.6 (purple), low-medium RCP4.5 (green), and high RCP8.5 (red) emissions scenarios.

from 1850 to 2005); thus, each ensemble simulation may sample about three to four AMO cycles as observed AMO typically has a time period of 60–80 years, although simulated AMO indices have multiple spectral peaks, such as around ~20 and at 30–50 years (discussed below). This leads to a sample of about 300–400 AMO cycles (or about ~38% of that

over 2006–99) from the 100 ensemble simulations. Thus, MPI-GE provides sufficient sampling of the AMO cycles for us to characterize its response to future external forcing, despite the small sampling by individual ensemble members.

3. Results

a. Characteristics of the model-simulated AMV

Before we examine model-projected future AMV changes, we need to know whether the MPI-ESM1.1 model can realistically simulate AMV's spatial pattern and time periods seen in observations. For comparison, we examine the observed and modeled AMV during the historical period from 1870 to 2018 (Fig. 1). In general, the model captures the observed AMV_{IV} and AMV_{EX} indices reasonably well, with the observed time series largely fitting within the ensemble spread (Fig. 1a). Different from the observed AMV_{IV} index (black line in Fig. 1a), the AMV_{IV} in the 100 ensemble members varies randomly in phase (Fig. 1a). This is expected since the temporal evolution of the internally generated AMV is realization dependent, so that it does not repeat itself among two different realizations (i.e., two different simulations). One particular realization (run #55, blue line in Fig. 1a) matches the observations remarkably well.

The SST anomaly patterns associated with the AMV_{IV} and AMV_{EX} in the model are broadly comparable to the
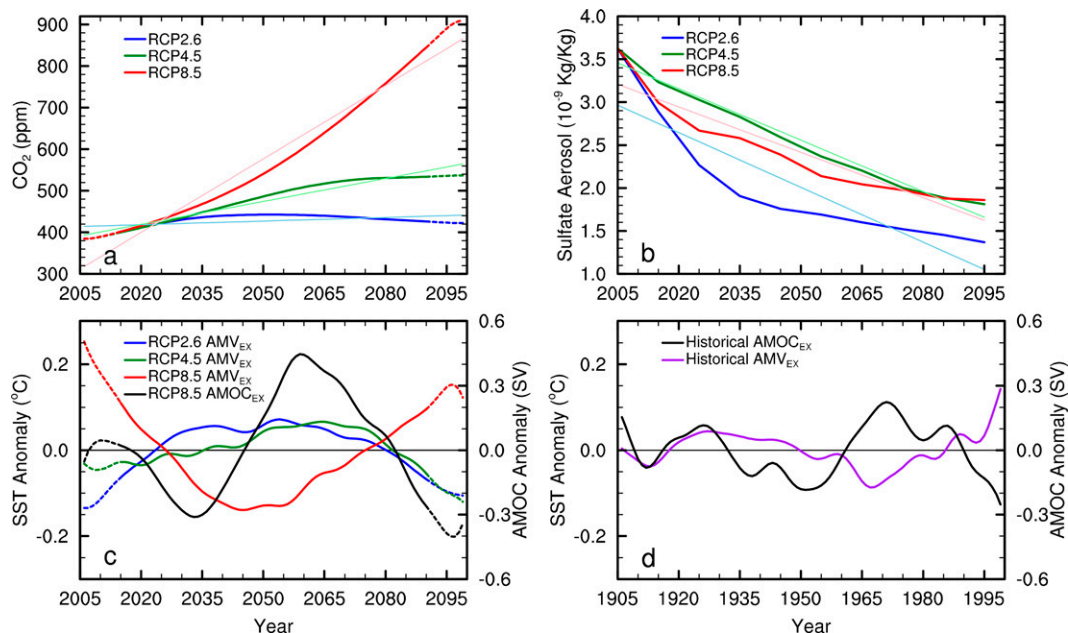

FIG. 3. Temporal variations of atmospheric CO_2 and aerosols, and NASST. (a) Time series of smoothed global-mean atmospheric CO_2 (ppm; solid lines) under the RCP2.6 (blue), RCP4.5 (green), and RCP8.5 (red) scenarios. The light lines represent the linear trend over 2006–99 for RCP2.6 (blue), RCP4.5 (green) and RCP8.5 (red). (b) As in (a), but for the mean sulfate aerosol concentrations (10^{-9} kg kg^{-1}) averaged over the North Atlantic (0°–60°N) derived from the RCP database version 2.0 (https://tntcat.iiasa.ac.at/RcpDb). The aerosol data are 10-yr averages centered at the middle of each decade. (c) Time series of the AMV_{EX} index (with the linear trend removed; °C) over 2006–99 under the RCP2.6, RCP4.5, and RCP8.5 scenarios from MPI-GE. The black line shows the smoothed $AMOC_{EX}$ under RCP8.5. The first and last 9 years, plotted using dashed lines, used mirrored data in the filtering and thus are less reliable. (d) As in (c), but for the historical period from 1906–99.
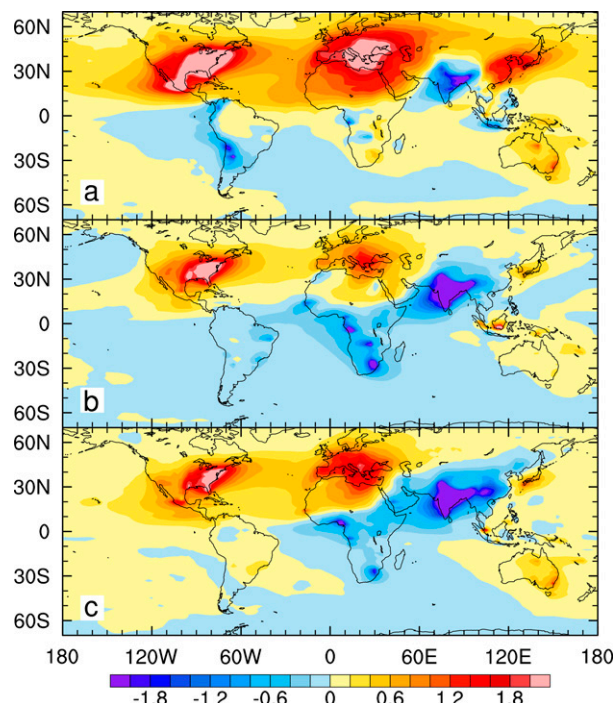
FIG. 4. Decadal anomalies in anthropogenic aerosol loadings under the three RCP scenarios. Annual-mean sulfate aerosol concentration anomalies for the decades centered at 2005, 2085, and 2095 (with high aerosol loading over the North Atlantic) relative to the decades centered at 2025, 2035, 2045, and 2055 (with low North Atlantic aerosol loading) under the (a) RCP2.6, (b) RCP4.5, and (c) RCP8.5 scenarios. The decadal-mean aerosol data were linearly detrended (i.e., with the 2005–105 linear trend removed) before calculating the anomalies.

observations during 1870–2018 (Fig. 1). For example, the internally generated SST patterns in the observations and model simulations also share similar features (spatial correlation $r > 0.67$), including a horseshoe-like pattern in the North Atlantic, cold anomaly (for a AMV_{IV} warm phase) in the South Atlantic and southern Indian Ocean and warm anomaly in the extratropical North Pacific, although the cold anomaly in the eastern tropical Pacific is not reproduced (Figs. 1b,c). The simulated AMV_{IV}-related historical patterns are also similar to those based on the PI control run (spatial correlation $r > 0.67$; Figs. 1c,d). These results suggest that our revised AMV_{IV} index is more conducive to represent the internally generated AMV. The model captures the NAWH in response to historical external forcing (spatial correlation $r > 0.86$), although the North Pacific (South Atlantic and Indian Ocean) SST response is overestimated (underestimated) (Figs. 1f,g). Maher et al. (2019) also showed that the observed variations in Northern Hemisphere oceans (e.g., AMOC) and over Europe were well represented in the MPI-GE. Overall, the model can reasonably simulate the observed AMV in terms of its spatial and temporal characteristics; thus MPI-GE can be used to investigate future changes over the North Atlantic Ocean.
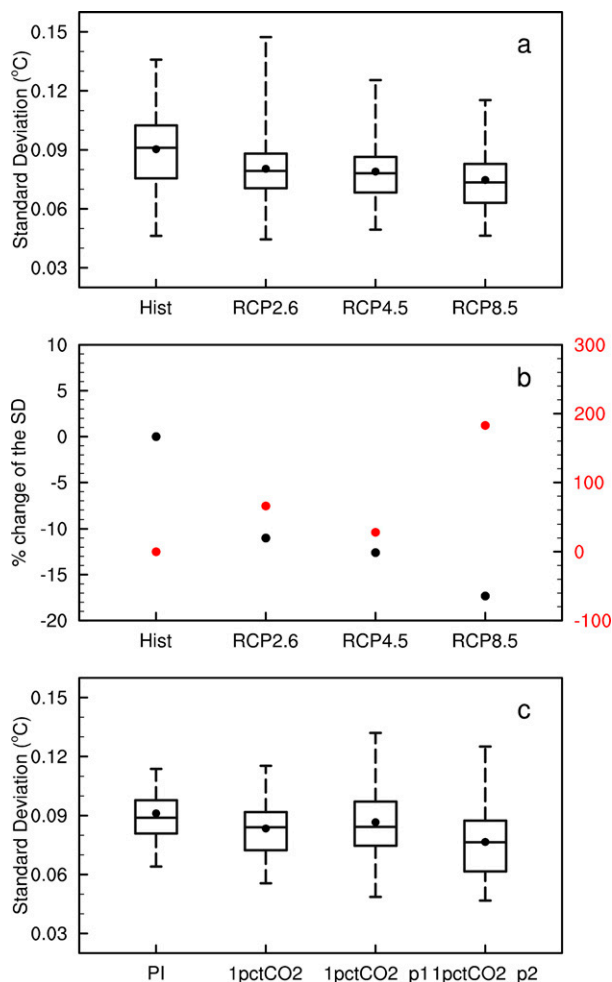

FIG. 5. Changes in the standard deviation (SD) of the AMV_{IV} and AMV_{EX} indices. (a) The SD of the AMV_{IV} index (°C) for the historical (1906–99) and three RCP (2006–99) simulations from MPI-GE. The ensemble-averaged mean SD of the AMV_{IV} index is shown by the black dots. The boxplots show the SD distribution among the ensemble members, with the inside line for the median, the box for the 25th–75th percentile range, and the whiskers for the maximum and minimum values. (b) Changes from the historical (Hist) simulations in the ensemble-averaged RCP/Hist ratio of the SD of the AMV_{IV} (black dots on the left y axis) or AMV_{EX} (red dots on the right y-axis). (c) As in (a), but for results from the PI control and 1pctCO2 simulations. 1pctCO2_p1 (1pctCO2_p2) represents the first (last) 100-yr simulations from the 1pctCO2 simulations. For the PI control run, 25 overlapped 150-yr segments, similar to the length of the 1pctCO2 runs, were used in estimating the SD. Results are similar if different overlapping is used in selecting the segments.

b. Responses of the AMV to future global warming

The future greenhouse gases (GHGs) are projected to rise rapidly, whereas anthropogenic aerosols are projected to decrease sharply in the twenty-first century (Lamarque et al. 2011; Smith and Bond 2014). For the periods after 2030, NASST differs substantially under the RCP2.6, RCP4.5, and RCP8.5 scenarios, and warms by 0.43°, 0.98°, and 2.36°C
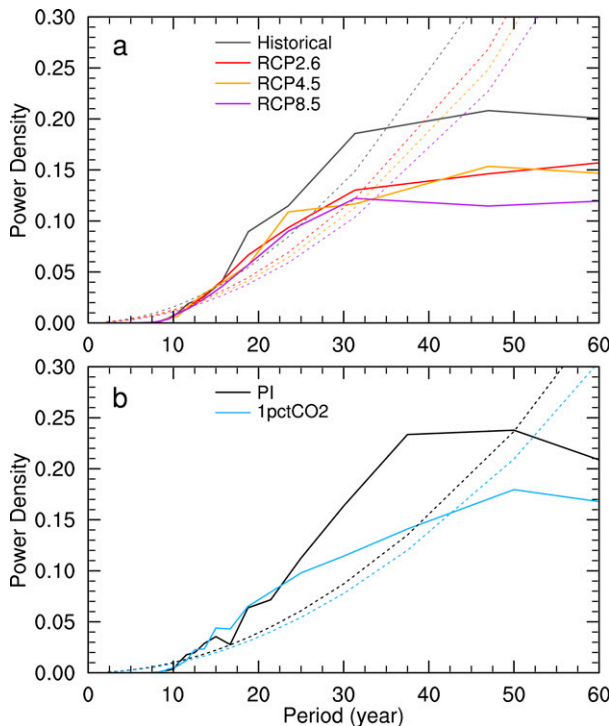
FIG. 6. Power spectrum comparisons of the AMV_{IV} index. (a) The ensemble-averaged power spectrum of the AMV_{IV} index from the historical (1906–99) and three RCP (2006–99) simulations. (b) As in (a), but from the PI control run and 1pctCO2 simulations. For the PI control run, 25 overlapped 150-yr segments (same as the length of the 1pctCO2 simulations) were used. Results are similar if different overlapping is used in selecting the segments. The upper 90% confidence internal of the red noise spectrum is shown as the thin dashed lines.

under these scenarios, respectively, by the 2090s relative to the 1990s (Fig. 2). We note that the NASST under the RCP8.5 scenario warms faster in the twenty-first century than that during the historical period, causing nonlinear variations over the whole period from 1870 to 2099 (Fig. 2). This would lead to multidecadal changes in the forced NASST relative to a long-term linear trend.

Different RCP scenarios lead to distinct decadal to multidecadal NASST variations relative to the linear trend from 2006 to 2099 resulting from nonlinear changes in the GHGs and aerosols (Figs. 3a,b and 4). For example, the AMV_{EX} under RCP8.5 exhibits cold phases from the mid-2020s to the 2070s and warm phases before the early 2020s and after the late 2070s (Fig. 3c). In contrast, the AMV_{EX} indices under RCP2.6 and RCP4.5 are highly anticorrelated with that under RCP8.5. In contrast, the sulfate aerosol loading over the North Atlantic shows similar multidecadal variations among the three scenarios, with reduced loading from about 2020 to 2070 (Fig. 3b) and high (low) loadings over North America and Europe (South Asia and Africa) during the high-loading decades relative to the low-loading decades (Fig. 4). Figure 4 shows that there exist substantial decadal variations in sulfate aerosols over the North Atlantic where they can affect SSTs,

although the largest variations are over Northern Hemisphere continents. These results indicate that different nonlinear changes in future external forcing under different scenarios (Figs. 3a,b) can produce different multidecadal variations in NASST relative to the long-term linear trend. These forced variations could be mixed up with internally generated AMV, just like in historical observations (Qin et al. 2020b).

To quantify the future AMV_{IV} and AMV_{EX} under global warming, we calculated their standard deviation (SD) and compared it with that in the historical runs. The SD of the AMV_{IV} decreases with future warming, on average by 11%, 13%, and 17% under RCP2.6, RCP4.5, and RCP8.5, respectively, albeit with a large spread (Figs. 5a,b). While these changes and the differences among the three scenarios are statistically insignificant ($p > 0.10$ based on F tests, except for RCP8.5), the fact that the ensemble mean AMV_{IV} weakens among all three scenarios and the weakening becomes stronger with larger warming suggests that the decrease is likely a robust response. Furthermore, 68, 65, and 78 out of the 100 runs show decreases in the SD of the AMV_{IV} under RCP2.6, RCP4.5, and RCP8.5, respectively. Thus, there exists a large chance ($>65\%$) that future warming can lead to weakened AMV_{IV}, although large internal variability may overshadow this weakening. We also compared the AMV_{IV} in the 150-yr 1pctCO2 simulations with that in the PI control run. The SD of the AMV_{IV} decreases by about 8% on average in the 1pctCO2 runs, with larger decreases in the later 100-yr period of the simulations (Fig. 5c). In contrast, the SD of the future AMV_{EX} tend to increase with global warming, approximately by 66%, 28%, and 183% under RCP2.6, RCP4.5, and RCP8.5, respectively (Fig. 5b). Thus, the RCP8.5 scenario produces the largest multidecadal variations (due to its nonlinear forcing), while the strength of the internally generated AMV decreases with the amount of future warming (thus AMV_{IV} decreases the most under RCP8.5).

Besides the amplitude, the AMV's period or frequency may also change. We calculated the power spectra of the AMV_{IV} index for each member from the historical and three RCP simulations (all for a 94-yr period) and show the ensemble mean of the power spectra in Fig. 6a, which indicates that the simulated historical AMV_{IV} have relatively high power for periods of 30 years and longer. The simulated AMV_{IV} under the future warming scenarios show reduced power on 20-yr and longer time scales, especially under RCP8.5, consistent with the reduction in its SD shown in Fig. 5. The lack of clear peaks in Fig. 6a may be partly due to the short record length of 94 years. Using a longer record of 150 years from the PI control run, the weak peak around 37 years in the AMV_{IV} index becomes more evident, with reduced power on 25-yr and longer time scales in the 1pctCO2 simulations (Fig. 6b). This further confirms the dampening effect of GHG-induced global warming on internally generated AMV.

Figure 7 shows the SST regression patterns against the standardized future AMV_{IV} and AMV_{EX} indices during 2006–99 under the three RCP scenarios. The internally generated AMV-related SST anomalies show comparable patterns among the scenarios with a horseshoe-like pattern in the North Atlantic and relatively weak anomalies elsewhere
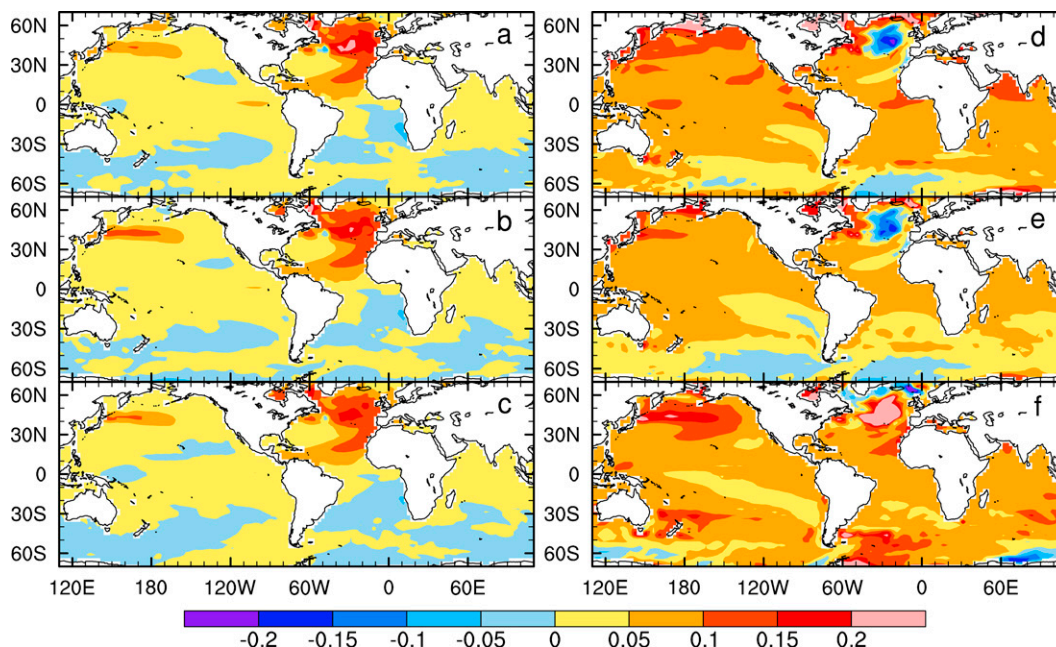
FIG. 7. SST regression patterns with the AMV_{IV} and AMV_{EX} indices. The ensemble-averaged spatial regression pattern (°C per one standard deviation of the AMV_{IV} index) obtained by regressing the low-pass filtered local SST anomalies from 2006 to 2099 onto the standardized AMV_{IV} index from individual (a) RCP2.6, (b) RCP4.5, and (c) RCP8.5 simulations from MPI-GE. (d)–(f) As in (a)–(c), but for regressed SST pattern onto the standardized AMV_{EX} index from RCP2.6, RCP4.5, and RCP8.5 simulations, respectively.

(Figs. 7a–c), and they are broadly similar to those seen in the historical and PI control simulations (Figs. 1i,j). This suggests that the spatial pattern of the internal AMV is not significantly affected by GHG-induced warming.

The imprints of the AMV_{EX} on the global SST fields are determined by the differences in the prescribed forcing under the three scenarios (Figs. 3a,b and 4) and associated responses. They exhibit considerable differences under the three RCP scenarios (Figs. 7d–f). There exists a warming hole in the subpolar North Atlantic under RCP2.6 and RCP4.5 (Figs. 7d,e) but enhanced warming under RCP8.5 (Fig. 7f). The SST pattern under RCP8.5 is broadly similar to the AMV_{IV}-associated SST fields and enhanced response in the northwestern North Pacific. However, if we do not linearly detrend externally forced NASST over 2006–99, the NAWH also exists in the regression pattern under RCP8.5. These results suggest that the externally forced SST variations are sensitive to the nonlinear changes in GHGs under different RCP scenarios, as aerosol forcing exhibits similar multidecadal variations around the North Atlantic under three RCP simulations (Figs. 3b and 4). That is, the nonlinear GHGs' influence may dominate over the multidecadal variations in future NASST, in particular in the subpolar North Atlantic.

c. Forced versus internal variations of the AMOC under global warming

Previous studies have indicated that the AMV_{IV}, which arises from internal dynamics of the climate system, is linked to changes in northward heat transport by the AMOC (Zhang et al. 2019), and climate models project weakening in both the mean (Collins et al. 2013; Reintges et al. 2017) and multidecadal variability (Cheng et al. 2016) of the AMOC under global warming. Given these, we also examine AMOC's multidecadal variability here. To separate the internally generated and externally forced multidecadal variations in future AMOC, we examine the $AMOC_{IV}$ and $AMOC_{EX}$, respectively. Figure 3c shows the $AMOC_{EX}$ index under the RCP8.5 scenario. Substantial forced $AMOC_{EX}$ variations up to 0.4 Sv ($1\,\mathrm{Sv} \equiv 1 \times 10^6\,\mathrm{m^3\,s^{-1}}$) exist in the model simulations. Similar to the AMV_{EX}, the forced $AMOC_{EX}$ also shows a larger amplitude under RCP8.5 than in the historical runs (Figs. 3c,d and 8b), suggesting increased nonlinear variations in future forcing. Like the AMV_{IV}, the $AMOC_{IV}$ indices in future ensemble simulations also exhibit different temporal evolution, and the AMV_{IV} and $AMOC_{IV}$ are significantly correlated with $AMOC_{IV}$ leading by 4–6 years (mean $r = 0.52$, $p < 0.05$).

Figures 8a and 8b show that the $AMOC_{IV}$ weakens on average by 48% from the historical to RCP8.5 twenty-first-century simulations, much larger than the 17% reduction in the AMV_{IV} (Fig. 5b) but consistent with AMOC's amplitude reduction reported by Cheng et al. (2016) under the extended RCP8.5 scenario. The ensemble-averaged power spectra of the $AMOC_{IV}$ (Fig. 8c) shows elevated power on 30-yr and longer time scales in the historical simulations, but greatly reduced power at these time scales under RCP8.5. Similar to the AMV_{IV} (Fig. 6), such a reduction of power on $\geq$30-yr time scales makes the variations on shorter time scales more important, which is qualitatively consistent with a shift toward
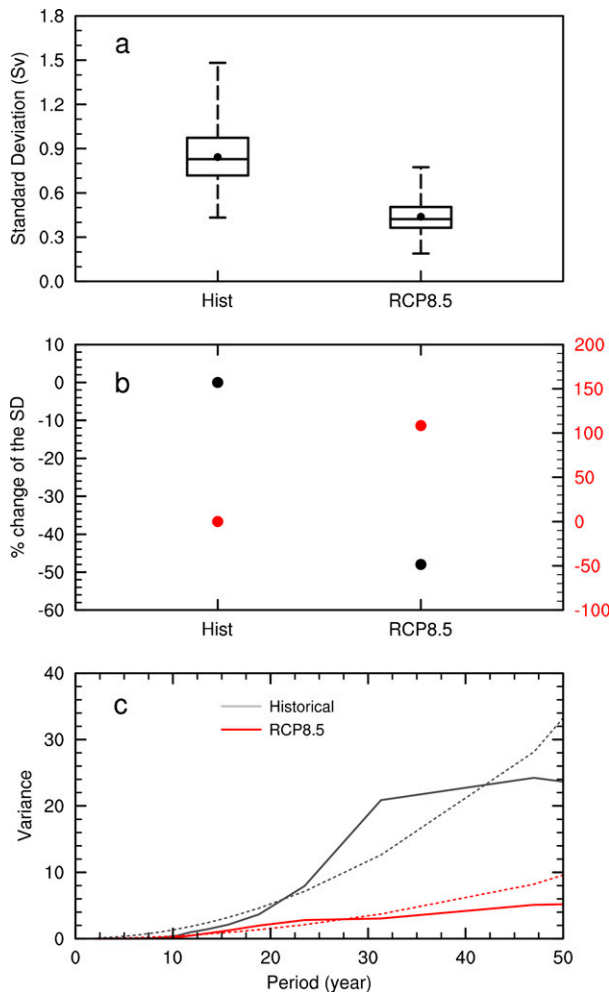
FIG. 8. The SD and power spectra of the $AMOC_{IV}$ and $AMOC_{EX}$ indices. (a) The SD of the $AMOC_{IV}$ index (Sv) from the historical (Hist; 1906–99) and RCP8.5 (2006–99) simulations. The ensemble-averaged SD of the $AMOC_{IV}$ is shown by the black dots. The boxplots show the distribution of the $AMOC_{IV}$ SD among the ensemble members, with the inside line for the median, the box for the 25th–75th percentile range, and the whiskers for the maximum and minimum values. (b) Ensemble-averaged percentage changes from the historical to future RCP8.5 simulations in the SD of the $AMOC_{IV}$ (black dots) and $AMOC_{EX}$ (red dots). (c) The ensemble-averaged power spectrum of the $AMOC_{IV}$ indices from the historical (1906–99) and RCP8.5 (2006–99) simulations. The upper 90% confidence internal of the red noise spectrum is shown as the thin dashed lines in (c).

higher frequency for $AMOC_{IV}$ reported by Cheng et al. (2016), who showed shortened periods for the interdecadal variability in AMOC in five CMIP5 models under extended RCP scenarios up to 2300. However, our results (Fig. 8c) show that future AMOC would still be dominated by variations on time scales of 20 years and longer without a clear peak, in contrast to a sharp peak around 17 years under RCP8.5 in Cheng et al. (2016). Besides the time difference (our analysis only covers the twenty-first century), we

explicitly removed the forced changes using the large ensemble mean from our $AMOC_{IV}$, while Cheng et al. (2016) used a statistical decomposition to remove the long-term trend that does not distinguish forced changes and internal variations.

Figure 9 shows the regression patterns of the Atlantic zonal-mean streamfunction against the standardized $AMOC_{IV}$ and $AMOC_{EX}$ indices. Consistent with Fig. 8, the internally generated AMOC anomalies, which peak around the climatological maximum near 40°N and 1.5-km depth, are much weaker in the RCP8.5 simulations for 2006–99 than in the historical period from 1906 to 1999, although their patterns are similar (Figs. 9a,b), consistent with the similar AMV_{IV}-related SST patterns (Figs. 7a,c). In contrast, the future forced AMOC anomalies are much stronger than the historical forced anomalies, with the maximum located near 1.9-km depth (Figs. 9d,e). We notice that the forced AMOC pattern during the historical period exhibits a sharp south–north contrast with small negative values over the South Atlantic (Fig. 9d), which is different from that for the forced pattern under RCP8.5 (Fig. 9e) and of the internal AMOC (Figs. 9a,b). The unique feature of the historical $AMOC_{EX}$ anomaly pattern is likely related to historical forcing changes, such as decadal changes in volcanic and anthropogenic aerosols (Qin et al. 2020b).

Different mechanisms have been proposed to explain the weakening multidecadal variability in NASST and AMOC. Cheng et al. (2016) suggested that an enhanced upper-ocean stratification under global warming could lead to an acceleration of oceanic Rossby waves, which may decrease both the amplitude and period of the AMOC. Wu and Liu (2020) suggested that the weakened forcing from atmospheric heat flux variability and the increased SST dampening rate under global warming may be responsible for the weakened AMOC and other climate changes over the North Atlantic. Deng and Dai (2021) showed that Arctic sea ice–air interactions amplify multidecadal variability in the Arctic and North Atlantic and such an amplification weakens under global warming as sea ice melts away, leading to weakened AMV and smaller multidecadal variability in AMOC. A detailed analysis of the processes leading to the AMV and AMOC changes is beyond the scope of this study.

d. Climatic impacts of the future AMV

We further examine the connection between the AMV and regional climates. For observations (Fig. 10a), the warm phase of the AMV_{IV} is characterized by a horseshoe-like, warm SST anomalies in the North Atlantic with largest amplitudes over the subpolar regions, together with warm anomalies over the North Pacific and most of North America and cold anomalies over midlatitude Eurasia and the South Atlantic (Fig. 10a). The cooling over Eurasia and the South Atlantic is particularly strong and widespread in boreal winter (Fig. 11a) but is weaker and less widespread in boreal summer (Fig. 12a), even though the warming over the North Atlantic is similar. The model reproduces the AMV_{IV}-related temperature patterns over the North Atlantic and North America for both annual and seasonal means, but the warming over the North America and the
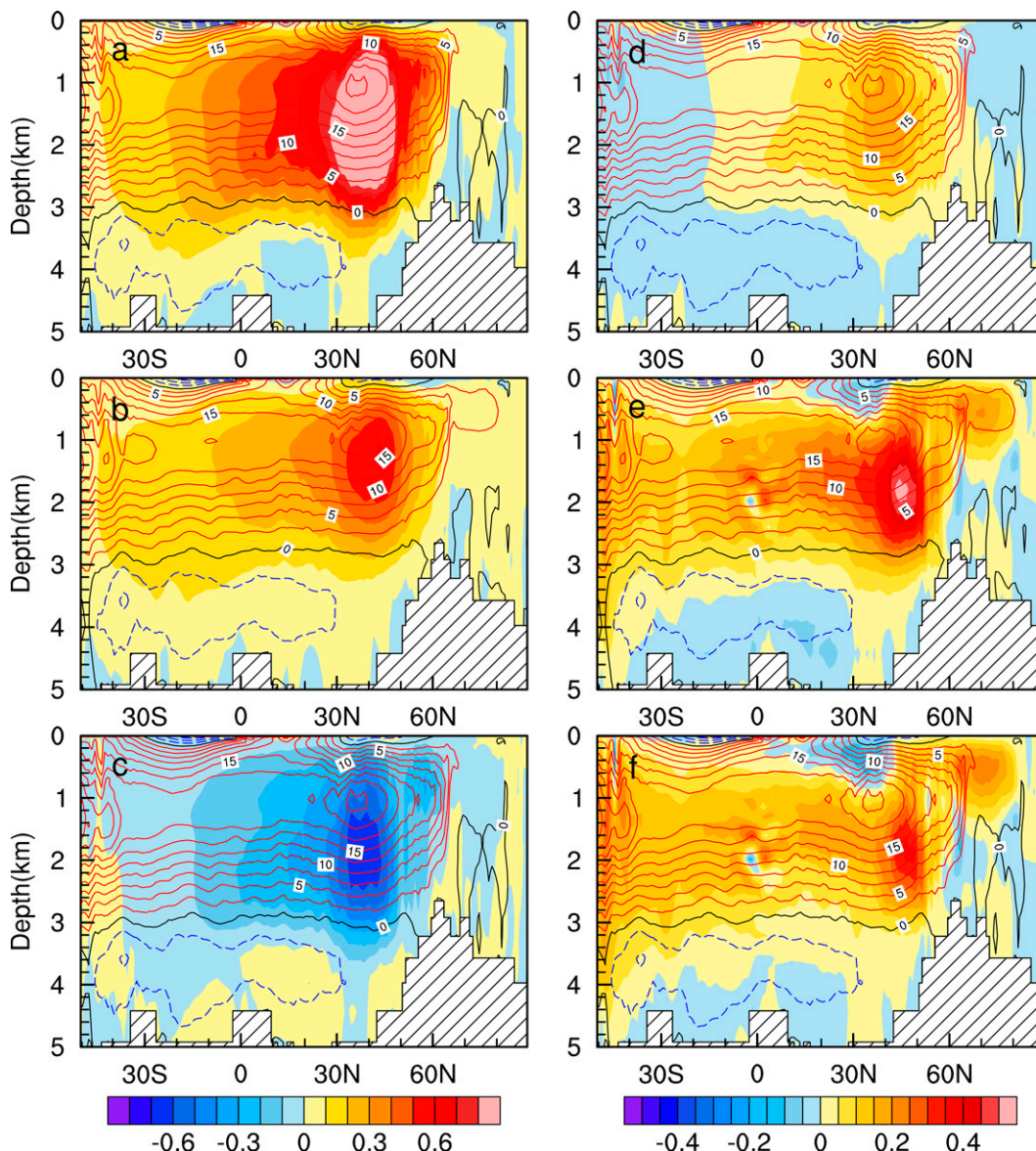
FIG. 9. Spatial patterns of the AMOC streamfunctions associated with the $AMOC_{IV}$ and $AMOC_{EX}$ indices. The ensemble-averaged spatial regression pattern (Sv per one standard deviation of the $AMOC_{IV}$ index) obtained by regressing the zonal-mean Atlantic meridional overturning circulation streamfunction anomalies onto the standardized $AMOC_{IV}$ index for the (a) historical (1906–99) and (b) RCP8.5 (2006–99) simulations from MPI-GE. Also shown are the climatological AMOC streamfunction (contours; Sv) to represent the mean AMOC pattern. (c) The difference of (b) minus (a). (d)–(f) As in (a)–(c), but for the $AMOC_{EX}$.

Pacific is weaker in the models than in observations (Figs. 10a,b, 11a,b, and 12a,b). The model fails to capture the strong cold anomalies over midlatitude Eurasia and the cooling over the South Atlantic is also too weak in the model, consistent with previous findings using CMIP3 or CMIP5 models (Ting et al. 2011; Lyu and Yu 2017).

The AMV_{IV}-related temperature anomaly pattern in the twenty-first century is comparable with that in the historical simulations (Figs. 10b–e, 11b,c, and 12b,c), with some differences in the magnitude. For example, the annual-mean

warming over North America under AMV_{IV}'s warm phase strengthens as the greenhouse gas forcing increases (Figs. 10b,c). In contrast, the Eurasian and North African temperature anomalies under the AMV_{IV}'s warm phase weakens when global warming increases (Figs. 10b,c), especially during boreal winter (Figs. 11b,c).

Figures 10–12 also show the composite anomalies of precipitation based on the AMV_{IV} index in observations and model simulations. In observations, the AMV_{IV}'s warm phase is associated with increased precipitation over the Sahel [mainly
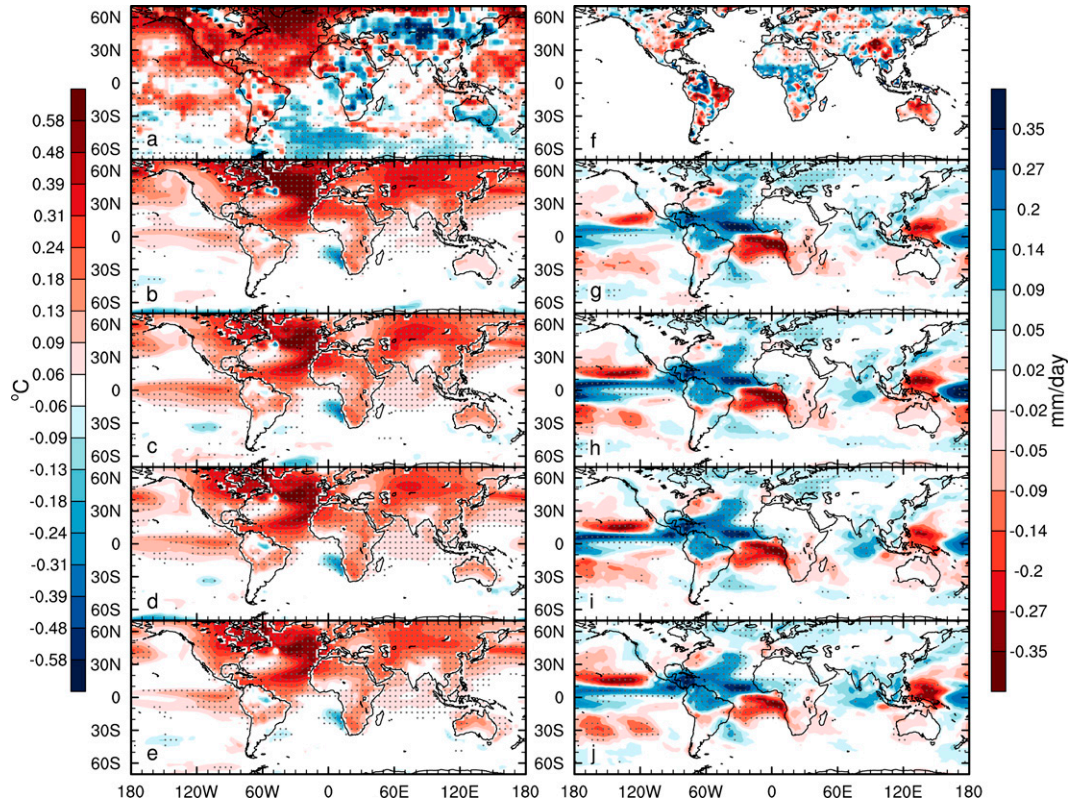
FIG. 10. Composite anomaly differences of annual temperature and precipitation between warm and cold AMV_{IV} phases. Composite anomaly differences of annual surface temperature (°C; SST over ocean and surface air temperature over land) between the positive and negative phases of the AMV_{IV} for (a) observations (1906–99), and the MPI-GE (b) historical (1906–99), (c) RCP2.6 (2006–99), (d) RCP4.5 (2006–99), and (e) RCP8.5 (2006–99) simulations from the MPI-GE. The AMV_{IV} warm (cold) phase is defined as the years with the AMV_{IV} index larger (lower) than one standard deviation, and the 100-member ensemble-averaged composite anomaly differences are used in (b)–(e). (f)–(j) As in (a)–(e), but for annual precipitation (mm day^{-1}). The stippling in (a) and (f) indicates that the differences are statistically significant at the 0.05 level based on a Student's t test considering autocorrelation, while the stippling in (b)–(e) and (g)–(j) represents 67 out of the 100 runs showing the same sign.

in June–August (JJA)], India, and the northern Amazon [mainly during December–February (DJF)], and decreased precipitation over the United States, central China (mainly in JJA), eastern Brazil, Australia (mainly in DJF), southern Africa, and eastern Europe and western Asia (Figs. 10f, 11d, and 12d). These precipitation anomaly patterns are consistent with previous findings (Zhang and Delworth 2006; Knight et al. 2006; Ting et al. 2011; Sutton and Dong 2012). The discrepancies between the modeled and observed precipitation are mainly located over Eurasia where the model shows weak wet anomalies while observations show significant drying during the AMV_{IV} positive phases (Fig. 10g). Similar precipitation responses to the AMV_{IV}'s warm phases also exist in the future scenario simulations, but with some differences in the magnitude (Figs. 10h–j).

Figure 13 shows the AMV_{EX}-related annual temperature and precipitation anomaly patterns. As expected, the warm phase of the AMV_{EX} is caused by positive external forcing anomalies that produce warming over most of the globe (especially over land), except the midlatitude North

Atlantic, where cold anomalies exist under the RCP2.6 and RCP4.5 scenarios (Figs. 13a,b) but not the RCP8.5 (Fig. 13c). The externally forced multidecadal SST variations are determined by the nonlinear changes in GHGs under different RCP scenarios, as the NAWH exists in the non-detrended SST change maps under RCP8.5 (not shown). For precipitation, the warm phase of the AMV_{EX} is associated with increased precipitation in the tropics but reduced precipitation in the subtropics (Figs. 13d–f). The tropical precipitation response is mediated by the SST change (Figs. 13a–c), similar to the warmer-get-wetter view (Xie et al. 2010). The AMV_{EX}-related temperature and precipitation patterns show some seasonal differences.

To quantify how the temperature anomalies under the warm phase of the AMV may change with anthropogenic warming, the surface temperature anomalies for the positive phase of the AMV_{IV} under RCP8.5 are contrasted with those in the historical runs (Fig. 14a). Negative temperature anomalies are seen over the midlatitude North Atlantic (decreased from 0.86°C in the historical runs to 0.53°C in
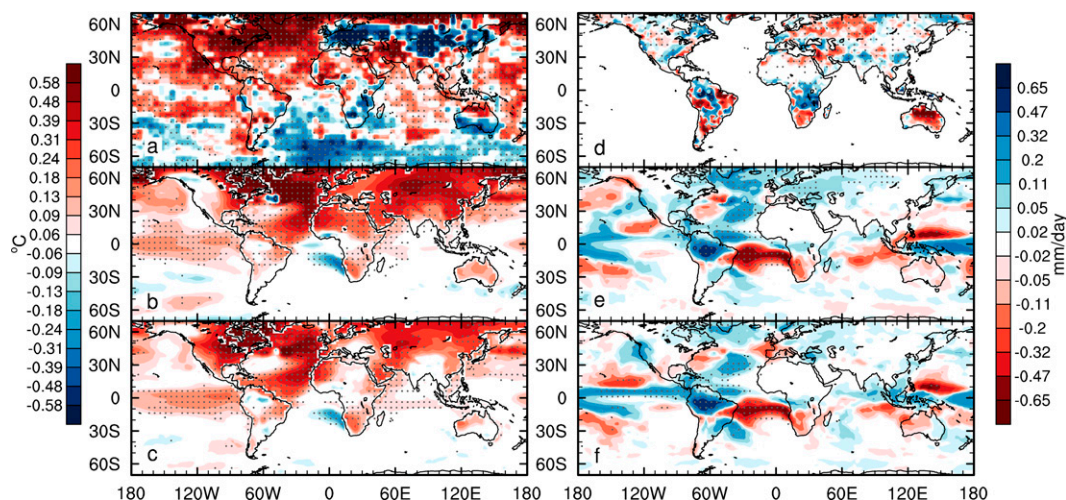
FIG. 11. As in Fig. 10, but for Northern Hemisphere winter (DJF) for (a),(d) observations, (b),(e) historical, and (c),(f) RCP8.5 simulations.

RCP8.5), Eurasia, and the North Pacific under the future warming scenario. This indicates weakened AMV_{IV} and $AMOC_{IV}$ variations under global warming with reduced SST and ocean circulation variations around the subpolar regions. The weakened temperature anomalies over Eurasia and northern Africa under the warm phase of the AMV_{IV} suggest that a warmer climate would not only reduce the amplitude of the AMV_{IV}, but also dampen the regional temperature anomalies associated with the AMV_{IV}. That is, when the AMV_{IV} amplitude decreases in a warmer climate, its associated regional (i.e., Eurasia and Africa) and global surface temperature anomalies could weaken. However, the AMV_{IV}-related North American temperature would enhance under global warming (Fig. 14a). For the impacts of the AMV_{EX}, the anthropogenic warming could produce stronger SST variations under RCP8.5 in the midlatitudes of the North Atlantic and North Pacific (Fig. 14c).

The AMV_{IV}-related precipitation over parts of North America and Eurasia reduces in a warmer climate (Fig. 14b). Our results show that the impact of the AMV_{IV} on global-mean precipitation would weaken by roughly 22% under the RCP8.5 simulation from 2006 to 2099 compared with the historical (1906–99) simulation, from 0.009 mm day^{-1} in the historical runs to 0.007 mm day^{-1} in the RCP8.5 simulations (Fig. 14b). Furthermore, the precipitation anomalies associated with the AMV_{EX} warm phase would weaken over most of the globe (Fig. 14d), with the global-mean anomaly decreasing from 0.012 mm day^{-1} in the historical runs to 0.009 mm day^{-1} in the RCP8.5 simulations.

We also repeat the same analysis for the comparison of the AMV_{IV}-associated temperature and precipitation anomalies between 1pctCO2 simulations and PI run (Figs. 14e,f), which show similar results to the changes between the historical and RCP8.5 simulations (Figs. 14a,b).
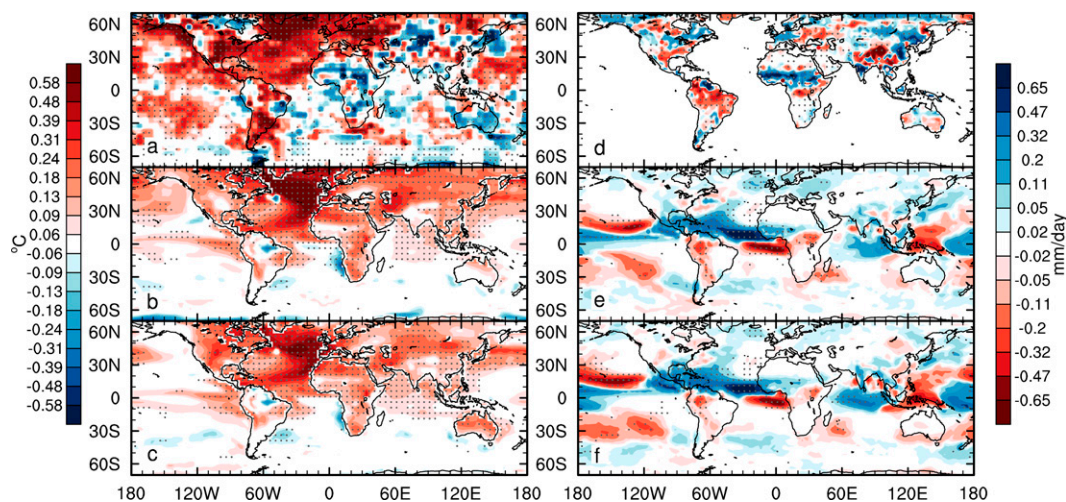

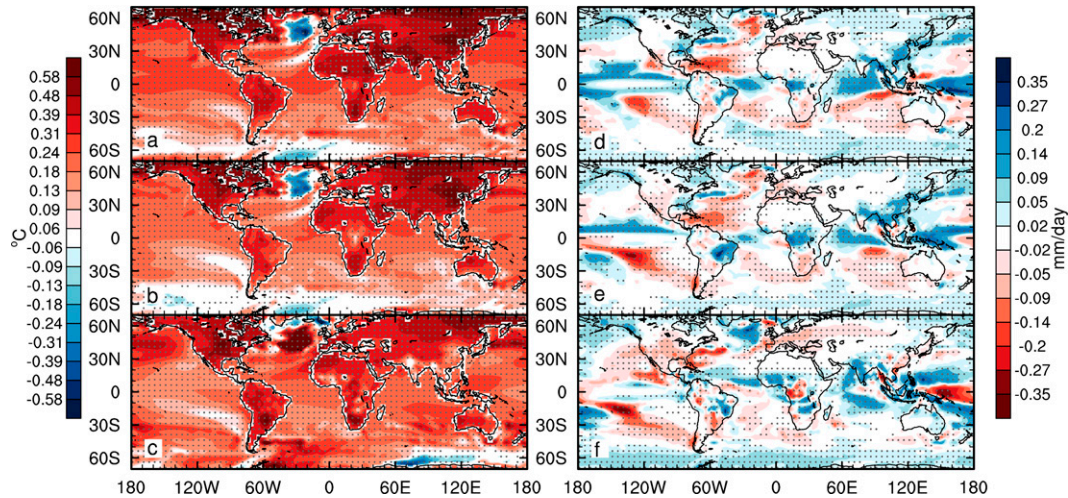FIG. 12. As in Fig. 11, but for Northern Hemisphere summer (JJA).

FIG. 13. Composite anomaly differences of annual temperature and precipitation between warm and cold AMV$_{EX}$ phases. Composite anomaly differences of annual surface temperature (°C, SST for ocean and air temperature for land) between the positive and negative phases of the AMV$_{EX}$ for (a) RCP2.6 (2006–99), (b) RCP4.5 (2006–99), and (c) RCP8.5 (2006–99) simulations from MPI-GE. (d)–(f) As in (a)–(c), but for annual precipitation (mm day^{-1}). The stippling indicates that the differences are statistically significant at the 0.05 level based on Student's t test considering autocorrelation.

4. Summary and discussion

In this study, we use an improved procedure to separate the internally generated and externally forced variations of the AMV (i.e., AMV$_{IV}$ and AMV$_{EX}$) in observations and model simulations from MPI-GE during the historical period and the twenty-first century. As the model reasonably simulates the observed AMV in terms of its spatial and temporal

characteristics from 1870 to 2018, the model can help us examine model-projected future AMV changes.

The future RCP scenarios show different nonlinear changes in the GHGs and aerosols, leading to distinct multidecadal NASST variations. These forced variations could be mixed up with the future AMV$_{IV}$ in individual realizations. Compared with the historical period, the standard deviation or amplitude of the future AMV$_{IV}$ tends to decrease with intensified
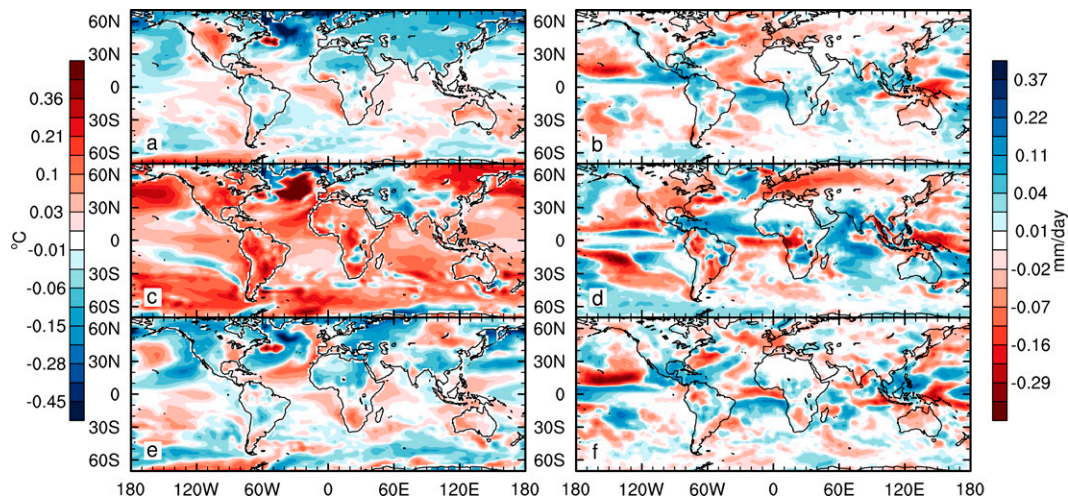

FIG. 14. Future changes in the temperature and precipitation anomaly patterns associated with the positive phase of the AMV$_{IV}$ and AMV$_{EX}$. (a) Ensemble-averaged difference between the RCP8.5 (2006–99) and historical (1906–99) simulations from MPI-GE in the composite anomaly of annual surface temperature (°C, SST over ocean and surface air temperature over land) associated with the AMV$_{IV}$'s positive phases. An AMV$_{IV}$'s positive phase is defined as the years with the AMV$_{IV}$ index larger than one standard deviation. (b) As in (a), but for annual precipitation (mm day^{-1}). (c),(d) As in (a) and (b), but for the positive phase of the AMO$_{EX}$. (e),(f) As in (a) and (b), but for the changes between the 1pctCO2 and preindustrial control simulations. For the PI control run, 25 overlapped 150-yr segments were used.

warming, by about 11%, 13%, and 17% under the RCP2.6, RCP4.5, and RCP8.5 scenarios, respectively. In contrast, the amplitude of the future AMO_{EX} is projected to increase, especially under the RCP8.5 scenario. The power spectra of the AMV_{IV} suggest a large reduction in the power of future AMV_{IV} on time scales of 30 years and longer, making the variations on 10–30 years relatively more important in the twenty-first century. These results are consistent with previous findings that the AMV_{IV} would have a weaker amplitude in a warmer climate, especially under RCP8.5. For the spatial pattern, the AMV_{IV}-related SST anomalies show comparable patterns among the scenarios with a horseshoe-like pattern in the North Atlantic and relatively weak anomalies elsewhere, indicating that the spatial pattern of the AMV_{IV} is not significantly affected by GHG-induced warming. The imprints of the AMV_{EX} on the global ocean exhibit striking differences under three RCP scenarios: There exists a warming hole in the subpolar North Atlantic under RCP2.6 and RCP4.5 scenarios, whereas enhanced warming is seen there under RCP8.5. Thus, the externally forced multidecadal SST variations are determined by the nonlinear changes in GHGs under different RCP scenarios, as the NAWH exists in the non-detrended SST change maps under RCP8.5.

Our results also show that the internal component of the AMOC (i.e., $AMOC_{IV}$) tends to have a smaller amplitude and reduced power on time scales of 30 years or longer under RCP8.5, consistent with the AMV_{IV} changes. On the other hand, the forced $AMOC_{EX}$ is projected to have a stronger amplitude. Thus, the $AMOC_{EX}$ and $AMOC_{IV}$ exhibit opposite responses to global warming in the twenty-first century in terms of their multidecadal amplitudes.

The weakening of the AMV_{IV} in a warmer climate implies its reduced impacts on global climate in the future. Our results show that the temperature anomaly patterns associated with a warm AMV_{IV} phase are roughly comparable between the historical and the future simulations, although the magnitude differ slightly. The AMV_{IV}-related temperature anomalies over Eurasia and North African (the United States) are weaker (stronger) as greenhouse gas forcing increases. The AMV_{IV}-related precipitation anomalies over South America and the Sahel are associated with the anomalous meridional shift of the Atlantic ITCZ. For the AMV_{EX}-related climatic pattern, the warm phase of the AMV_{EX} is caused by positive external forcing anomalies that cause warming anomalies over land and most oceans, except the subpolar North Atlantic where cold anomaly is seen under RCP2.6 and RCP4.5. The AMV_{EX}-related global-mean land temperature and precipitation variations would weaken in the twenty-first century compared with the historical period from 1906 to 1999.

In this study, we adopted a revised procedure to define the AMV_{IV} and AMV_{EX}. An implicit assumption is that externally forced responses and internally generated variations are linearly separable. However, our results show that long-term anthropogenic warming might affect the decadal to multidecadal variations of internally generated NASST (i.e., there may be interactions between the forced responses and internal variability). A future rapid warming by the end of twenty-first century could influence the amplitude of the AMV_{IV}, or ENSO

and the IPO as demonstrated in previous studies (Cai et al. 2015; Xu and Hu 2018; Wu and Liu 2020; Caesar et al. 2018; Keil et al. 2020). Thus, potential nonlinear interactions between the anthropogenic warming and decadal NASST variations may be significant. Further, the model does not capture some of the observed features associated with the AMV (e.g., the model shows a consistent warm anomaly over Eurasia while observations show a cold anomaly over central Eurasia during a positive AMV phase). Given the relative short sampling from observations, it is unclear whether the cold anomaly over central Eurasia, the Atlantic sector of the Southern Ocean, and Africa in JJA is a robust feather of the AMV_{IV} or it is related to something else (e.g., the IPO; Dai et al. 2015) that may be aliased into the limited sampling of the AMV_{IV} positive and negative phases. Thus, there is still some uncertainty regarding whether the discrepancy is due to model deficiencies or sampling errors. Furthermore, we should also note that our results are based on one model only. Further efforts to explore the influence of anthropogenic warming on the AMV using other state-of-the-art climate models (Deser et al. 2020) are needed. Thus, one needs to interpret our results with these caveats in mind. Nevertheless, we think that our MPI-GE based results provide a first-order estimate of the likely changes in the internally generated and externally forced components of the AMV in the twenty-first century.

REFERENCES

Bellomo, K., L. N. Murphy, M. A. Cane, A. C. Clement, and L. M. Polvani, 2018: Historical forcings as main drivers of the Atlantic multidecadal variability in the CESM large ensemble. *Climate Dyn.*, **50**, 3687–3698, https://doi.org/10.1007/s00382-017-3834-3.

Bellucci, A., A. Mariotti, and S. Gualdi, 2017: The role of forcings in the twentieth-century North Atlantic multidecadal

variability: The 1940–75 North Atlantic cooling case study. *J. Climate*, **30**, 7317–7337, https://doi.org/10.1175/JCLI-D-16-0301.1.

Booth, B. B. B., 2015: Why the Pacific is cool. *Science*, **347**, 952, https://doi.org/10.1126/science.aaa4840.

——, N. J. Dunstone, P. R. Halloran, T. Andrews, and N. Bellouin, 2012: Aerosols implicated as a prime driver of twentieth-century North Atlantic climate variability. *Nature*, **484**, 228–232, https://doi.org/10.1038/nature10946.

Caesar, L., S. Rahmstorf, A. Robinson, G. Feulner, and V. Saba, 2018: Observed fingerprint of a weakening Atlantic Ocean overturning circulation. *Nature*, **556**, 191–196, https://doi.org/10.1038/s41586-018-0006-5.

Cai, W., and Coauthors, 2015: ENSO and greenhouse warming. *Nat. Climate Change*, **5**, 849–859, https://doi.org/10.1038/nclimate2743.

Cheng, J., Z. Liu, S. Zhang, W. Liu, L. Dong, P. Liu, and H. Li, 2016: Reduced interdecadal variability of Atlantic meridional overturning circulation under global warming. *Proc. Natl. Acad. Sci. USA*, **113**, 3175–3178, https://doi.org/10.1073/pnas.1519827113.

Chylek, P., J. D. Klett, G. Lesins, M. K. Dubey, and N. Hengartner, 2014: The Atlantic multidecadal oscillation as a dominant factor of oceanic influence on climate. *Geophys. Res. Lett.*, **41**, 1689–1697, https://doi.org/10.1002/2014GL059274.

Clement, A., K. Bellomo, L. N. Murphy, M. A. Cane, T. Mauritsen, G. Rädel, and B. Stevens, 2015: The Atlantic multidecadal oscillation without a role for ocean circulation. *Science*, **350**, 320–324, https://doi.org/10.1126/science.aab3980.

Collins, M., and Coauthors, 2010: The impact of global warming on the tropical Pacific Ocean and El Niño. *Nat. Geosci.*, **3**, 391–397, https://doi.org/10.1038/ngeo868.

——, and Coauthors, 2013: Long-term climate change: Projections, commitments and irreversibility. *Climate Change 2013: The Physical Science Basis*, T. F. Stocker et al., Eds., Cambridge University Press, 1029–1136.

Dai, A., and C. E. Bloecker, 2019: Impacts of internal variability on temperature and precipitation trends in large ensemble simulations by two climate models. *Climate Dyn.*, **52**, 289–306, https://doi.org/10.1007/s00382-018-4132-4.

——, A. Hu, G. A. Meehl, W. M. Washington, and W. G. Strand, 2005: Atlantic thermohaline circulation in a coupled circulation model: Unforced variations versus forced changes. *J. Climate*, **18**, 3270–3293, https://doi.org/10.1175/JCLI3481.1.

——, J. C. Fyfe, S.-P. Xie, and X. Dai, 2015: Decadal modulation of global surface temperature by internal climate variability. *Nat. Climate Change*, **5**, 555–559, https://doi.org/10.1038/nclimate2605.

Delworth, T. L., and M. E. Mann, 2000: Observed and simulated multidecadal variability in the Northern Hemisphere. *Climate Dyn.*, **16**, 661–676, https://doi.org/10.1007/s003820000075.

——, and K. W. Dixon, 2006: Have anthropogenic aerosols delayed a greenhouse gas-induced weakening of the North Atlantic thermohaline circulation? *Geophys. Res. Lett.*, **33**, L02606, https://doi.org/10.1029/2005GL024980.

——, and F. Zeng, 2016: The impact of the North Atlantic Oscillation on climate through its influence on the Atlantic meridional overturning circulation. *J. Climate*, **29**, 941–962, https://doi.org/10.1175/JCLI-D-15-0396.1.

——, ——, L. Zhang, R. Zhang, G. A. Vecchi, and X. Yang, 2017: The central role of ocean dynamics in connecting the North Atlantic Oscillation to the extratropical component of

the Atlantic multidecadal oscillation. *J. Climate*, **30**, 3789–3805, https://doi.org/10.1175/JCLI-D-16-0358.1.

Deng, J., and A. Dai, 2021: Sea ice–air interactions amplify multidecadal variability in the North Atlantic and Arctic region. Research Square, preprint, https://doi.org/10.21203/rs.3.rs-81129/v1.

Deser, C., and A. S. Phillips, 2021: Defining the internal component of Atlantic multidecadal variability in a changing climate. *Geophys. Res. Lett.*, **48**, e2021GL095023, https://doi.org/10.1029/2021GL095023.

——, and Coauthors, 2020: Insights from Earth system model initial-condition large ensembles and future prospects. *Nat. Climate Change*, **10**, 277–286, https://doi.org/10.1038/s41558-020-0731-2.

Drijfhout, S., W. Hazeleger, F. Selten, and R. Haarsma, 2008: Future changes in internal variability of the Atlantic meridional overturning circulation. *Climate Dyn.*, **30**, 407–419, https://doi.org/10.1007/s00382-007-0297-y.

Enfield, D. B., A. M. Mestas-Nuñez, and P. J. Trimble, 2001: The Atlantic multidecadal oscillation and its relation to rainfall and river flows in the continental U.S. *Geophys. Res. Lett.*, **28**, 2077–2080, https://doi.org/10.1029/2000GL012745.

Folland, C. K., T. N. Palmer, and D. E. Parker, 1986: Sahel rainfall and worldwide sea temperatures, 1901–85. *Nature*, **320**, 602–607, https://doi.org/10.1038/320602a0.

Frankcombe, L. M., M. H. England, M. E. Mann, and B. A. Steinman, 2015: Separating internal variability from the externally forced climate response. *J. Climate*, **28**, 8184–8202, https://doi.org/10.1175/JCLI-D-15-0069.1.

——, ——, J. B. Kajtar, M. E. Mann, and B. A. Steinman, 2018: On the choice of ensemble mean for estimating the forced signal in the presence of internal variability. *J. Climate*, **31**, 5681–5693, https://doi.org/10.1175/JCLI-D-17-0662.1.

Ghosh, R., W. A. Müller, J. Baehr, and J. Bader, 2017: Impact of observed North Atlantic multidecadal variations to European summer climate: A linear baroclinic response to surface heating. *Climate Dyn.*, **48**, 3547–3563, https://doi.org/10.1007/s00382-016-3283-4.

Giorgetta, M. A., and Coauthors, 2013: Climate and carbon cycle changes from 1850 to 2100 in MPI-ESM simulations for the Coupled Model Intercomparison Project phase 5. *J. Adv. Model. Earth Syst.*, **5**, 572–597, https://doi.org/10.1002/jame.20038.

Haustein, K., and Coauthors, 2019: A limited role for unforced internal variability in twentieth-century warming. *J. Climate*, **32**, 4893–4917, https://doi.org/10.1175/JCLI-D-18-0555.1.

Hua, W., A. Dai, and M. Qin, 2018: Contributions of internal variability and external forcing to the recent Pacific decadal variations. *Geophys. Res. Lett.*, **45**, 7084–7092, https://doi.org/10.1029/2018GL079033.

——, ——, L. Zhou, M. Qin, and H. Chen, 2019: An externally-forced decadal rainfall seesaw pattern over the Sahel and southeast Amazon. *Geophys. Res. Lett.*, **46**, 923–932, https://doi.org/10.1029/2018GL081406.

——, M. Qin, A. Dai, L. Zhou, H. Chen, and W. Zhang, 2021: Reconciling human and natural drivers of the tripole pattern of multidecadal summary temperature variations over Eurasia. *Geophys. Res. Lett.*, **48**, e2021GL093971, https://doi.org/10.1029/2021GL093971.

Kay, J. E., and Coauthors, 2015: The Community Earth System Model (CESM) large ensemble project: A community resource for studying climate change in the presence of

internal climate variability. *Bull. Amer. Meteor. Soc.*, **96**, 1333–1349, https://doi.org/10.1175/BAMS-D-13-00255.1.

Keil, P., T. Mauritsen, J. Jungclaus, C. Hedemann, D. Olonscheck, and R. Ghosh, 2020: Multiple drivers of the North Atlantic warming hole. *Nat. Climate Change*, **10**, 667–671, https://doi.org/10.1038/s41558-020-0819-8.

Kerr, R. A., 2000: A North Atlantic climate pacemaker for the centuries. *Science*, **288**, 1984–1985, https://doi.org/10.1126/science.288.5473.1984.

Knight, J. R., R. J. Allan, C. K. Folland, M. Vellinga, and M. E. Mann, 2005: A signature of persistent natural thermohaline circulation cycles in observed climate. *Geophys. Res. Lett.*, **32**, L20708, https://doi.org/10.1029/2005GL024233.

——, C. K. Folland, and A. A. Scaife, 2006: Climate impacts of the Atlantic multidecadal oscillation. *Geophys. Res. Lett.*, **33**, L17706, https://doi.org/10.1029/2006GL026242.

Kushnir, Y., 1994: Interdecadal variations in North Atlantic sea surface temperature and associated atmospheric conditions. *J. Climate*, **7**, 141–157, https://doi.org/10.1175/1520-0442(1994)007<0141:IVINAS>2.0.CO;2.

Lamarque, J.-F., G. P. Kyle, M. Meinshausen, K. Riahi, S. J. Smith, D. P. van Vuuren, A. J. Conley, and F. Vitt, 2011: Global and regional evolution of short-lived radiatively-active gases and aerosols in the representative concentration pathways. *Climatic Change*, **109**, 191–212, https://doi.org/10.1007/s10584-011-0155-0.

Liu, W., A. V. Fedorov, S.-P. Xie, and S. Hu, 2020: Climate impacts of a weakened Atlantic meridional overturning circulation in a warming climate. *Sci. Adv.*, **6**, eaaz4876, https://doi.org/10.1126/sciadv.aaz4876.

Lu, R., B. Dong, and H. Ding, 2006: Impact of the Atlantic multidecadal oscillation on the Asian summer monsoon. *Geophys. Res. Lett.*, **33**, L24701, https://doi.org/10.1029/2006GL027655.

Lyu, K., and J.-Y. Yu, 2017: Climate impacts of the Atlantic multidecadal oscillation simulated in the CMIP5 models: A reevaluation based on a revised index. *Geophys. Res. Lett.*, **44**, 3867–3876, https://doi.org/10.1002/2017GL072681.

Maher, N., and Coauthors, 2019: The Max Planck Institute Grand Ensemble: Enabling the exploration of climate system variability. *J. Adv. Model. Earth Syst.*, **11**, 2050–2069, https://doi.org/10.1029/2019MS001639.

Mann, M. E., and K. A. Emanuel, 2006: Atlantic hurricane trends linked to climate change. *Eos, Trans. Amer. Geophys. Union*, **87**, 233–241, https://doi.org/10.1029/2006EO240001.

Martin, E. R., C. D. Thorncroft, and B. B. Booth, 2014: The multidecadal Atlantic SST–Sahel rainfall teleconnection in CMIP5 simulations. *J. Climate*, **27**, 784–806, https://doi.org/10.1175/JCLI-D-13-00242.1.

Monerie, P.-A., J. Robson, B. Dong, and D. Hodson, 2021: Role of the Atlantic multidecadal variability in modulating East Asian climate. *Climate Dyn.*, **56**, 381–398, https://doi.org/10.1007/s00382-020-05477-y.

Morice, C. P., J. J. Kennedy, N. A. Rayner, and P. D. Jones, 2012: Quantifying uncertainties in global and regional temperature change using an ensemble of observational estimates: The HadCRUT4 data set. *J. Geophys. Res.*, **117**, D08101, https://doi.org/10.1029/2011JD017187.

Murphy, L. N., K. Bellomo, M. Cane, and A. Clement, 2017: The role of historical forcings in simulating the observed Atlantic multidecadal oscillation. *Geophys. Res. Lett.*, **44**, 2472–2480, https://doi.org/10.1002/2016GL071337.

O'Reilly, C. H., T. Woollings, and L. Zanna, 2017: The dynamical influence of the Atlantic multidecadal oscillation on

continental climate. *J. Climate*, **30**, 7213–7230, https://doi.org/10.1175/JCLI-D-16-0345.1.

Otterå, O. H., M. Bentsen, H. Drange, and L. Suo, 2010: External forcing as a metronome for Atlantic multidecadal variability. *Nat. Geosci.*, **3**, 688–694, https://doi.org/10.1038/ngeo955.

Qasmi, S., C. Cassou, and J. Boé, 2017: Teleconnection between Atlantic multidecadal variability and European temperature: Diversity and evaluation of the Coupled Model Intercomparison Project phase 5 models. *Geophys. Res. Lett.*, **44**, 11 140–11 149, https://doi.org/10.1002/2017GL074886.

Qin, M., A. Dai, and W. Hua, 2020a: Aerosol-forced multidecadal variations across all ocean basins in models and observations since 1920. *Sci. Adv.*, **6**, eabb0425, https://doi.org/10.1126/sciadv.abb0425.

——, ——, and ——, 2020b: Atlantic multidecadal variability resulted from internal variability and volcanic and anthropogenic aerosols since 1870. *Geophys. Res. Lett.*, **47**, e2020GL089504, https://doi.org/10.1029/2020GL089504.

Rayner, N. A., D. E. Parker, E. B. Horton, C. K. Folland, L. V. Alexander, D. P. Rowell, E. C. Kent, and A. Kaplan, 2003: Global analyses of sea surface temperature, sea ice, and night marine air temperature since the late nineteenth century. *J. Geophys. Res.*, **108**, 4407, https://doi.org/10.1029/2002JD002670.

Reintges, A., T. Martin, M. Latif, and N. S. Keenlyside, 2017: Uncertainty in twenty-first century projections of the Atlantic meridional overturning circulation in CMIP3 and CMIP5 models. *Climate Dyn.*, **49**, 1495–1511, https://doi.org/10.1007/s00382-016-3180-x.

Ruprich-Robert, Y., R. Msadek, F. Castruccio, S. Yeager, T. Delworth, and G. Danabasoglu, 2017: Assessing the climate impacts of the observed Atlantic multidecadal variability using the GFDL CM2.1 and NCAR CESM1 global coupled models. *J. Climate*, **30**, 2785–2810, https://doi.org/10.1175/JCLI-D-16-0127.1.

——, T. Delworth, R. Msadek, F. Castruccio, S. Yeager, and G. Danabasoglu, 2018: Impacts of the Atlantic multidecadal variability on North American summer climate and heat waves. *J. Climate*, **31**, 3679–3700, https://doi.org/10.1175/JCLI-D-17-0270.1.

Schlesinger, M. E., and N. Ramankutty, 1994: An oscillation in the global climate system of period 65–70 years. *Nature*, **367**, 723–726, https://doi.org/10.1038/367723a0.

Schneider, U., A. Becker, P. Finger, A. Meyer-Christoffer, M. Ziese, and B. Rudolf, 2014: GPCC's new land surface precipitation climatology based on quality-controlled in situ data and its role in quantifying the global water cycle. *Theor. Appl. Climatol.*, **115**, 15–40, https://doi.org/10.1007/s00704-013-0860-x.

Si, D., and A. Hu, 2017: Internally generated and externally forced multidecadal oceanic modes and their influence on the summer rainfall over East Asia. *J. Climate*, **30**, 8299–8316, https://doi.org/10.1175/JCLI-D-17-0065.1.

Smith, S. J., and T. C. Bond, 2014: Two hundred fifty years of aerosols and climate: The end of the age of aerosols. *Atmos. Chem. Phys.*, **14**, 537–549, https://doi.org/10.5194/acp-14-537-2014.

Steinman, B. A., M. E. Mann, and S. K. Miller, 2015: Atlantic and Pacific multidecadal oscillations and Northern Hemisphere temperatures. *Science*, **347**, 988–991, https://doi.org/10.1126/science.1257856.

Sun, C., J. Li, and F.-F. Jin, 2015: A delayed oscillator model for the quasi-periodic multidecadal variability of the NAO.

Climate Dyn., **45**, 2083–2099, https://doi.org/10.1007/s00382-014-2459-z.

Sutton, R. T., and D. L. R. Hodson, 2005: Atlantic Ocean forcing of North American and European summer climate. *Science*, **309**, 115–118, https://doi.org/10.1126/science.1109496.

——, and B. Dong, 2012: Atlantic Ocean influence on a shift in European climate in the 1990s. *Nat. Geosci.*, **5**, 788–792, https://doi.org/10.1038/ngeo1595.

Tandon, N. F., and P. J. Kushner, 2015: Does external forcing interfere with the AMOC's influence on North Atlantic sea surface temperature? *J. Climate*, **28**, 6309–6323, https://doi.org/10.1175/JCLI-D-14-00664.1.

Terray, L., 2012: Evidence for multiple drivers of North Atlantic multi-decadal climate variability. *Geophys. Res. Lett.*, **39**, L19712, https://doi.org/10.1029/2012GL053046.

Ting, M., Y. Kushnir, R. Seager, and C. Li, 2009: Forced and internal twentieth-century SST trends in the North Atlantic. *J. Climate*, **22**, 1469–1481, https://doi.org/10.1175/2008JCLI2561.1.

——, ——, ——, and ——, 2011: Robust features of Atlantic multi-decadal variability and its climate impacts. *Geophys. Res. Lett.*, **38**, L17705, https://doi.org/10.1029/2011GL048712.

Trenberth, K. E., and D. J. Shea, 2006: Atlantic hurricanes and natural variability in 2005. *Geophys. Res. Lett.*, **33**, L12704, https://doi.org/10.1029/2006GL026894.

Vecchi, G. A., T. L. Delworth, and B. Booth, 2017: Origins of Atlantic decadal swings. *Nature*, **548**, 284–285, https://doi.org/10.1038/nature23538.

Wang, C., S. Dong, A. T. Evan, G. R. Foltz, and S.-K. Lee, 2012: Multidecadal covariability of North Atlantic sea surface temperature, African dust, Sahel rainfall, and Atlantic hurricanes. *J. Climate*, **25**, 5404–5415, https://doi.org/10.1175/JCLI-D-11-00413.1.

Watanabe, M., and H. Tatebe, 2019: Reconciling roles of sulphate aerosol forcing and internal variability in Atlantic multidecadal

climate changes. *Climate Dyn.*, **53**, 4651–4665, https://doi.org/10.1007/s00382-019-04811-3.

Wu, S., and Z. Liu, 2020: Decadal variability in the North Pacific and North Atlantic under global warming: The weakening response and its mechanism. *J. Climate*, **33**, 9181–9193, https://doi.org/10.1175/JCLI-D-19-1012.1.

——, ——, J. Cheng, and C. Li, 2018: Response of North Pacific and North Atlantic decadal variability to weak global warming. *Adv. Climate Change Res.*, **9**, 95–101, https://doi.org/10.1016/j.accre.2018.03.001.

Wu, Z., and N. E. Huang, 2009: Ensemble empirical mode decomposition: A noise-assisted data analysis method. *Adv. Adapt. Data Anal.*, **1**, 1–41, https://doi.org/10.1142/S1793536909000047.

Xie, S., C. Deser, G. A. Vecchi, J. Ma, H. Teng, and A. T. Wittenberg, 2010: Global warming pattern formation: Sea surface temperature and rainfall. *J. Climate*, **23**, 966–986, https://doi.org/10.1175/2009JCLI3329.1.

Xu, Y., and A. Hu, 2018: How would the 21st-century warming influence Pacific decadal variability and its connection to North American rainfall: Assessment based on a revised procedure for IPO/PDO. *J. Climate*, **31**, 1547–1563, https://doi.org/10.1175/JCLI-D-17-0319.1.

Zhang, R., and T. L. Delworth, 2006: Impact of Atlantic multidecadal oscillations on India/Sahel rainfall and Atlantic hurricanes. *Geophys. Res. Lett.*, **33**, L17712, https://doi.org/10.1029/2006GL026267.

——, R. Sutton, G. Danabasoglu, Y.-O. Kwon, R. Marsh, S. G. Yeager, D. E. Amrhein, and C. M. Little, 2019: A review of the role of the Atlantic meridional overturning circulation in Atlantic multidecadal variability and associated climate impacts. *Rev. Geophys.*, **57**, 316–375, https://doi.org/10.1029/2019RG000644.